Appendix A

SUPPORTING INFORMATION FOR CHAPTER 4

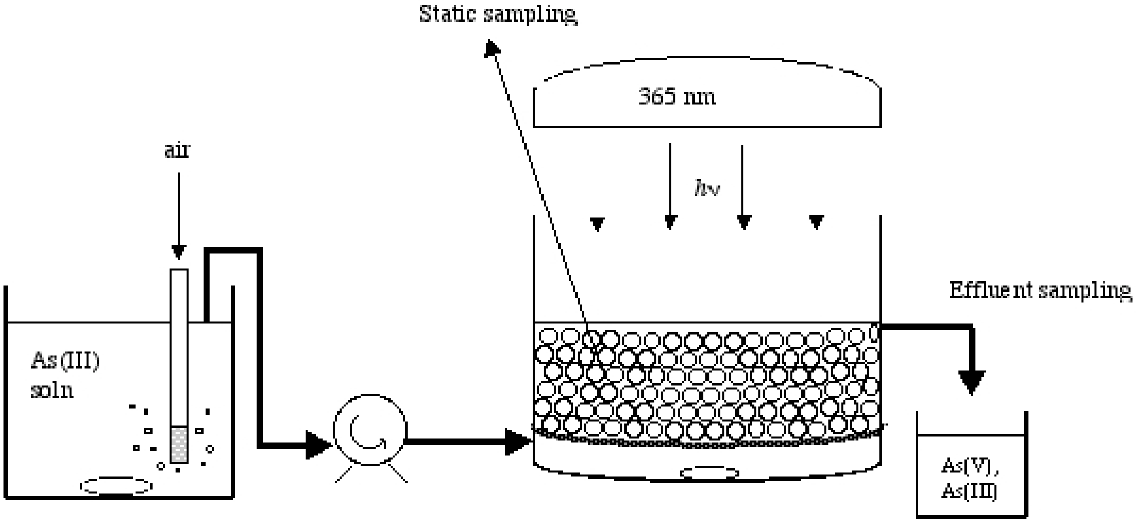

Figure A.1. Schematic of the fixed-bed, flow-through reactor.

Table A.1. Conditions for modeling (Geochemist's Workbench 6.0, X1t). Inlet composition was identical to initial composition for the first model, whereas the inlet composition for the lateral flow model was defined as the output of the upward flow model. Porosity = 0.42, run time = 100 min, specific discharge = 0.0007928–0.00357 cm s^{-1} (corresponding to average residence times ranging from 26.25 to 5.85 min). For upward flow model: length = 2.5 cm, width = height = 5.8 cm. For lateral flow model: length = 0.75–5.95 cm, width = 5.8 cm, height = 0.5 cm.

Component	**Initial Composition**
H_2O	1 kg (solvent)
$As(OH)_4^-$	2.64 µmolar
NO_3^-	5 mmolar, used for charge balance
Na^+	5 mmolar
H^+	pH = 6.4
$O_{2(aq)}$	0.26 mM
AsO_4^{--}	1 e-20 µmolar

Table A.2. Contributing fraction of the six nodes to the total rate constant used in the model. Each node represents one bead layer, where influent solution progresses upward from node 1 to node 6. Fractional values for nodes 4–6 were assigned according to the fraction of incident light passing through each bead layer; fractions for nodes 1–3 were set arbitrarily because transmitted light was below the limit of quantitation.

Node, *i*	**Fraction of total rate constant, *f*(*i*)**
1	0.00352
2	0.00469
3	0.00916
4	0.0194
5	0.0918
6	0.872

The default rate law in Geochemist's Workbench (GWB) was overridden using scripts which assigned the first-order rate law as a function of node *i*:

Rate = Wmass * rate_con * molality("As(OH)3") * *f*(*i*) * 6,

Where Wmass is the mass of water (i.e., it adjusts for node volume) and rate_con is the overall reactor rate constant inputted into the GWB interface. The rate was multiplied by a factor of 6 to adjust for the 6 nodes.

The variable length of the second GWB model was designed to incorporate 0.1 cm of upward flow through the top bead layer in addition to a variable distance representing lateral flow toward the reactor outlet. Since the top bead layer was cylindrical, the lateral flow took place across a circular cross section. This cross section was segmented into 5 circular arc sections of equal length on the diameter, and the midpoint of each section was taken to represent all effluent issuing from that section (Figure A.2). Model outputs were calculated for each of the 5 path lengths and multiplied by the percent area contribution values to get a weighted average $[\mathrm{As(III)}]_{\mathrm{out}}$.

Experimental flow was determined to be laminar based on Reynolds numbers ranging from 0.21 to 0.94.

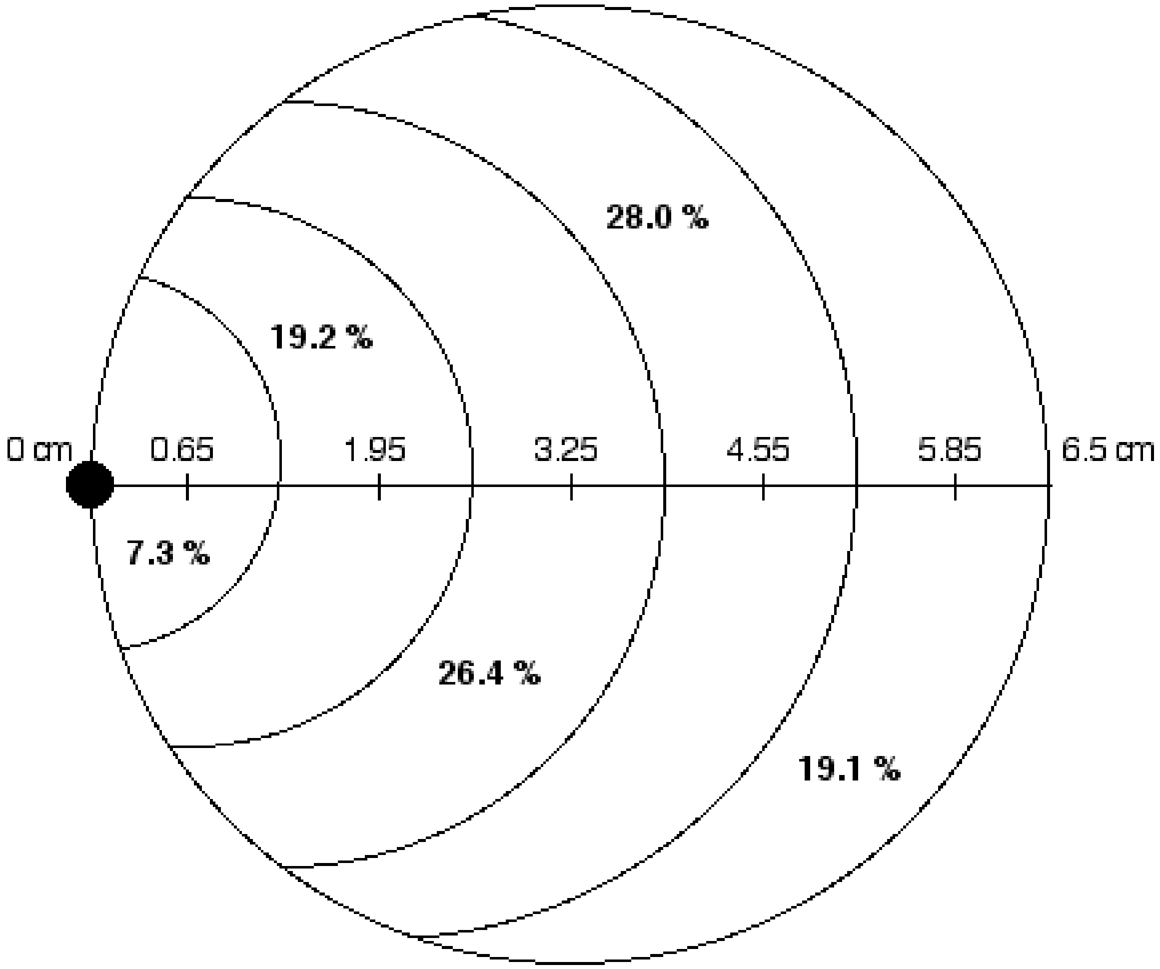

Figure A.2. The five sections of the top bead layer used in modeling reactor output and their corresponding contributions to total area. Path length used in the model is equal to the distance from the outlet (0) plus 0.1 cm for upward flow. Model outputs for each section were multiplied by the percent section area to calculate a weighted average $[\mathrm{As(III)}]_{\mathrm{out}}$.

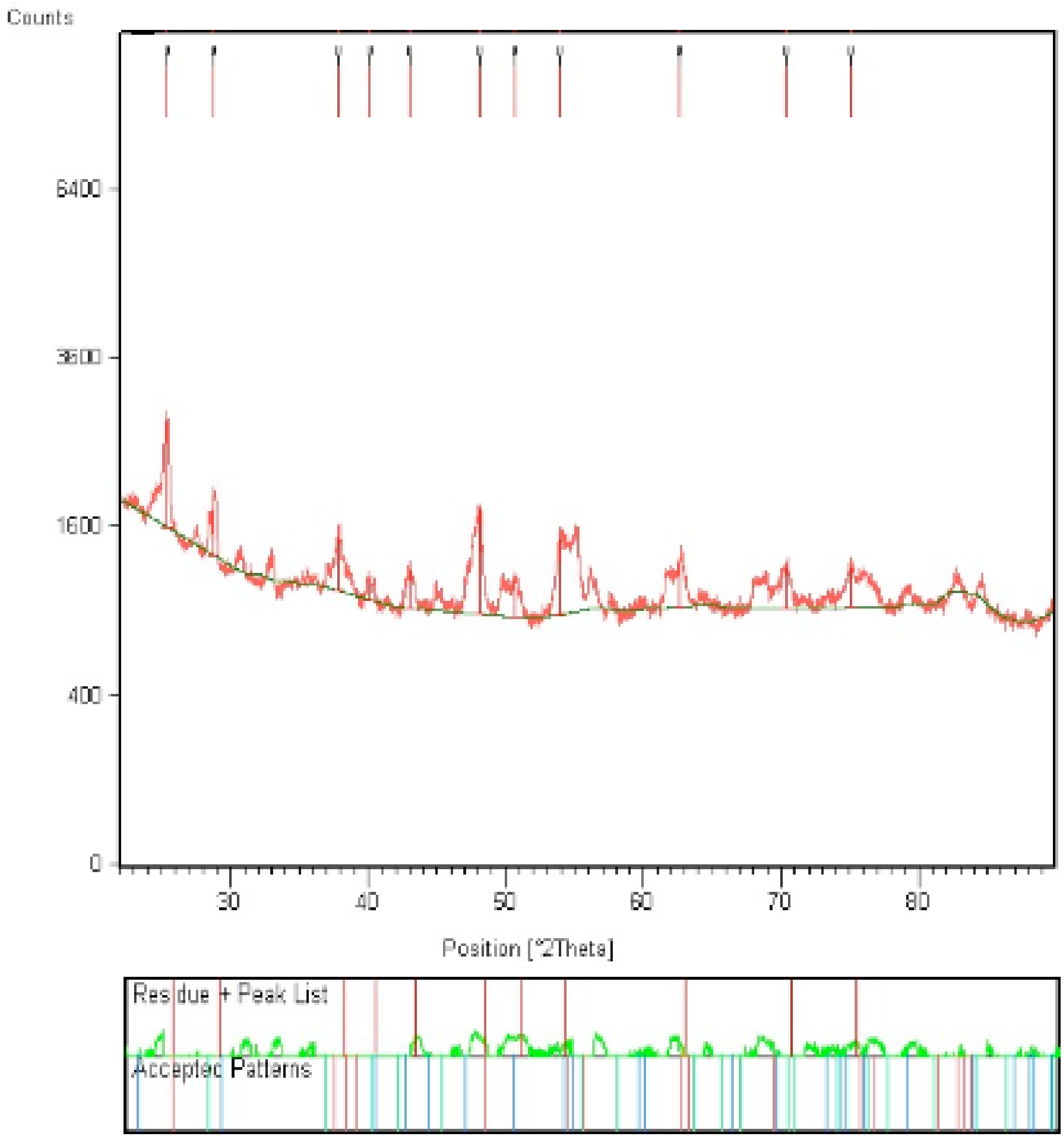

Figure A.3. X-ray diffractogram for a bead coated 8 times with P25/sol-gel. Conditions: step size = 0.0167, time per step = 240. Accepted patterns correspond to anatase (red), rutile (green), and quartz (blue).

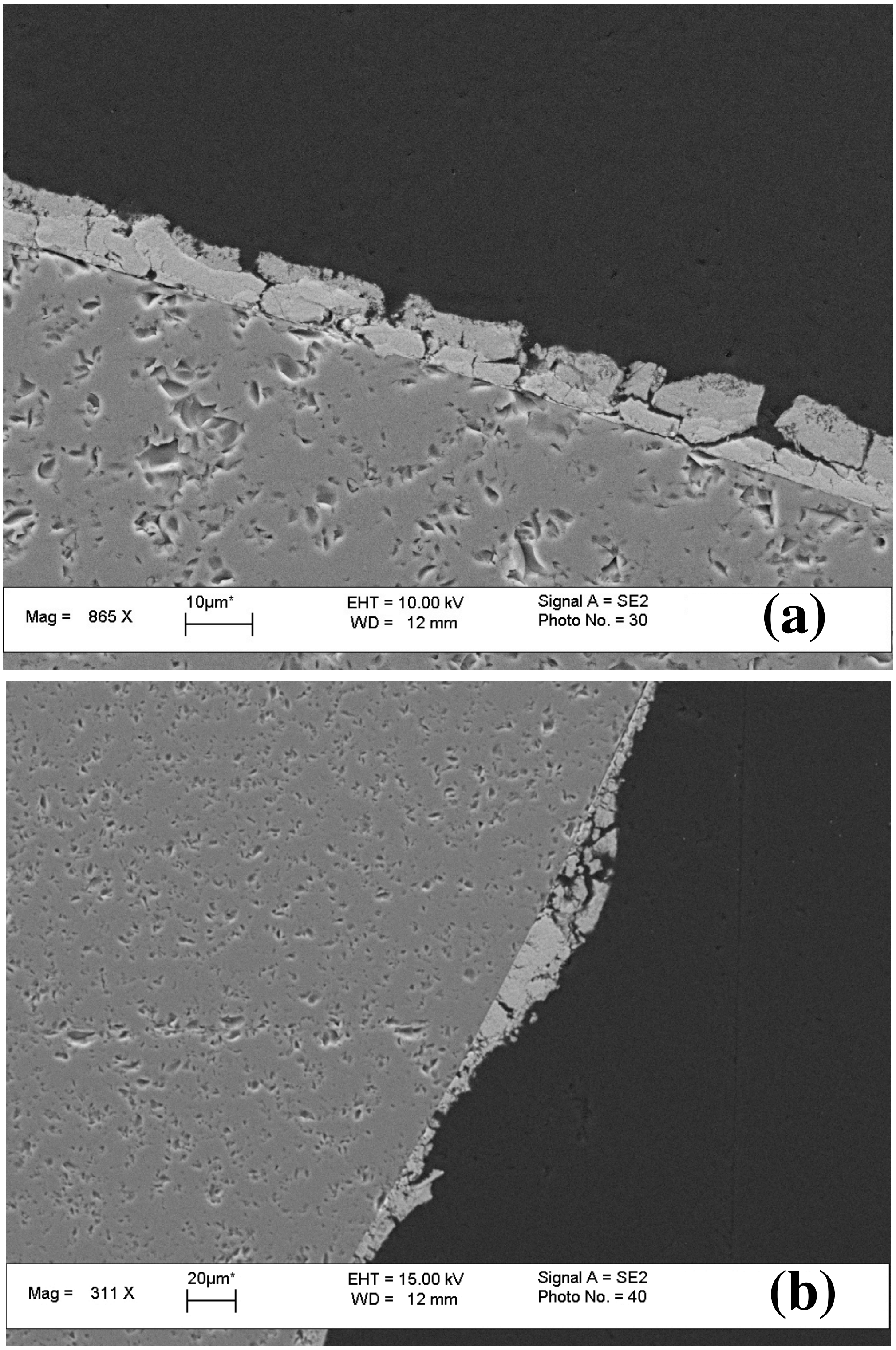

Figure A.4. SEM micrographs of cross sections of beads coated 8 times (a) and 4 times (b). Conditions: electron high tension = 10 kV (a) or 15 kV (b); working distance = 12 mm, SE2 detector, 865x (a) or 311x (b) magnification.

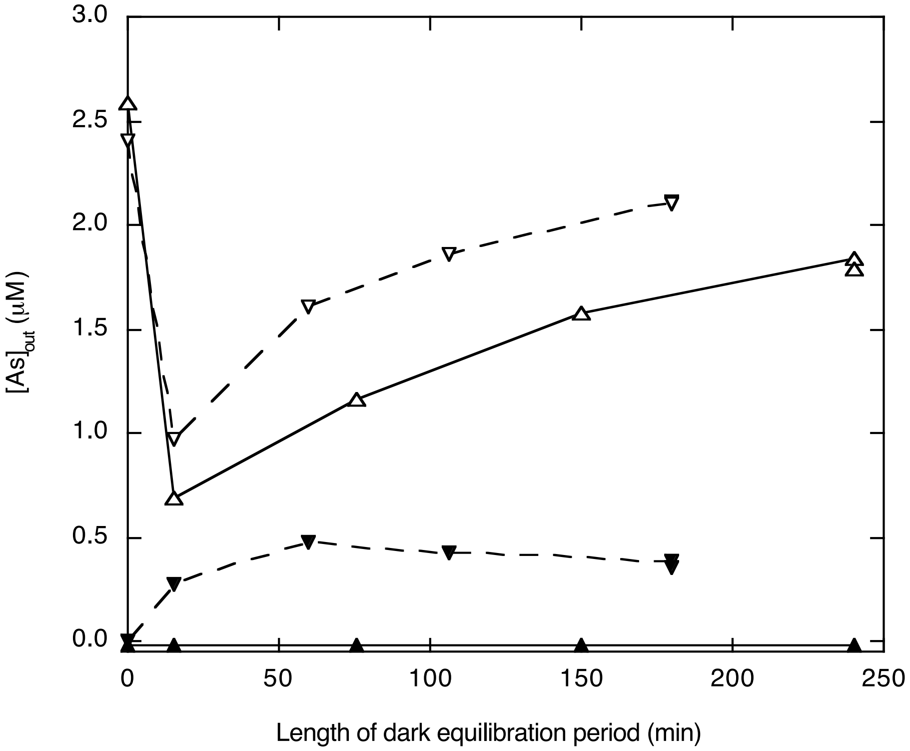

Figure A.5. Effluent As(III) (open symbols) and As(V) (closed symbols) concentrations during the dark sorption equilibration period for new beads (△,▲) and beads used 3 times previously (▽,▼). Influent concentrations are plotted at *t* = 0. Conditions: pH 6.4, $[As(III)]_{in}$ = 2.6 μM, $[NaNO_3]$ = 5 mM, average residence time = 10 min, 4x coated beads.

Table A.3. Conditions and values of steady-state $[As(III)]_{out}$ and $[As(V)]_{out,\ t\ =\ 180\ min}$ for all experiments. Groundwater is abbreviated by GW.

Matrix	Flow Rate (mL min^{-1})	Number of TiO_2 Coatings	$[As(III)]_0$ (μM)	Number of Times Beads Used Previously	Steady-State $[As(III)]_{out}$ (μM)	$[As(V)]_{out}$ at 180 min (μM)
5 mM $NaNO_3$	7.2	4	2.6	2	0.76	1.8
5 mM $NaNO_3$	7.2	4	2.6	4	0.75	2.0
5 mM $NaNO_3$	7.2	4	2.6	4	0.61	2.1
5 mM $NaNO_3$	7.2	4	2.6	6	0.65	1.8
5 mM $NaNO_3$	4.2	4	2.6	0	0.29	0.72
5 mM $NaNO_3$	4.2	4	2.6	0	0.39	0.82
5 mM $NaNO_3$	4.2	4	2.6	1	0.29	1.1
5 mM $NaNO_3$	4.2	4	2.6	3	0.32	1.9
5 mM $NaNO_3$	4.2	4	2.6	5	0.42	2.3
5 mM $NaNO_3$	2.7	4	2.6	5	0.26	2.2
5 mM $NaNO_3$	2.7	4	2.6	6	0.22	2.6
5 mM $NaNO_3$	2.7	4	2.6	7	0.30	2.0
5 mM $NaNO_3$	1.6	4	2.6	1	0.20	0.95
5 mM $NaNO_3$	1.6	4	2.6	2	0.32	1.4
5 mM $NaNO_3$	7.2	4	8.3	3	3.0	5.3
5 mM $NaNO_3$	7.2	4	8.3	5	2.8	5.5
5 mM $NaNO_3$	7.2	4	8.3	6	3.2	4.5
5 mM $NaNO_3$	7.2	4	0.56	4	0.13	0.56
5 mM $NaNO_3$	7.2	4	0.56	6	0.13	0.54
5 mM $NaNO_3$	7.2	4	0.56	7	0.13	0.55
5 mM $NaNO_3$	7.2	8	2.6	3	0.85	1.0
5 mM $NaNO_3$	7.2	8	2.6	4	0.88	1.2
5 mM $NaNO_3$	7.2	8	2.6	5	0.75	1.7
5 mM $NaNO_3$	7.2	1	2.6	0[a]	1.1	1.6
5 mM $NaNO_3$	7.2	1	2.6	1[a]	0.77	1.9
5 mM $NaNO_3$	7.2	1	2.6	2[a]	0.65	1.8
synthetic GW	4.2	4	2.6	0[a]	0.86	1.6
synthetic GW	4.2	4	2.6	1[a]	0.68	1.8
synthetic GW	4.2	4	2.6	2[a]	0.51	2.0
high F/PO_4 GW	4.2	4	2.6	0[a]	0.74	1.5
high F/PO_4 GW	4.2	4	2.6	1[a]	0.75	1.7
synthetic GW[b]	4.2	4	2.6	2[a]	0.22	2.0

a. Beads were equilibrated with As(III) / As(V) solution overnight and rinsed several times with water prior to their first use.

b. Natural sunlight was used for irradiation rather than a 365 nm UV lamp.

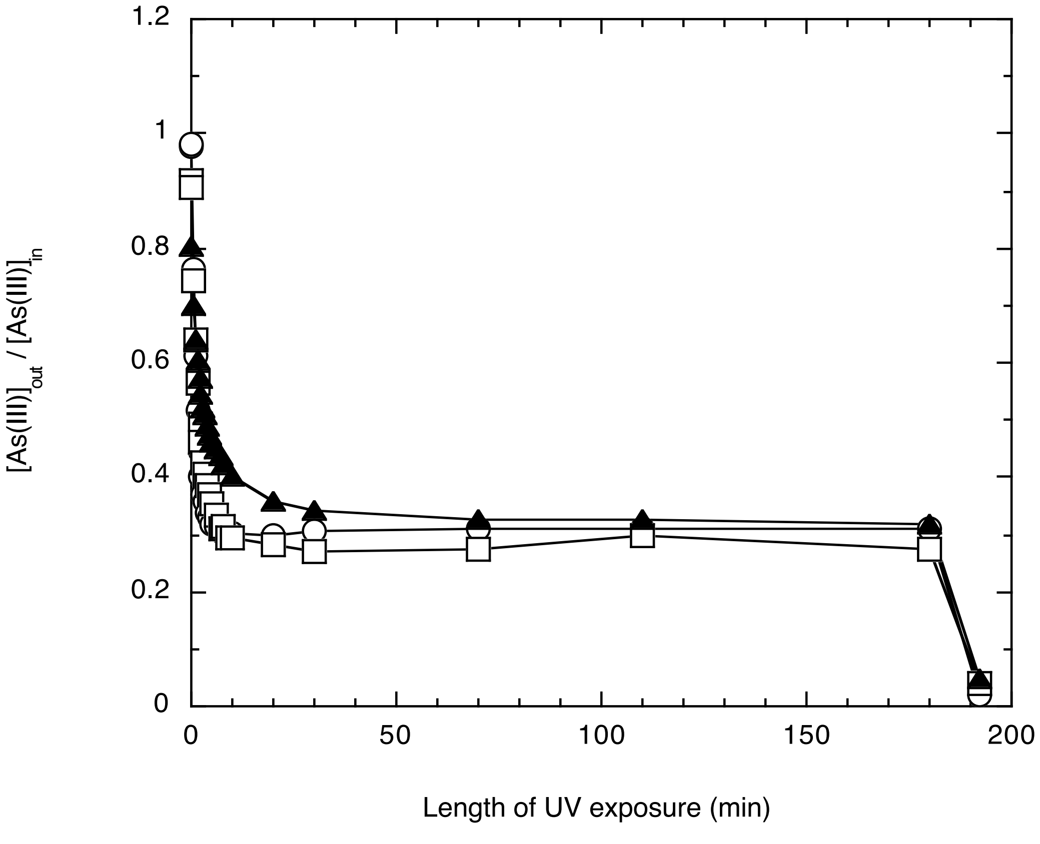

Figure A.6. As(III) oxidation performance for beads coated 1 (○), 4 (□), and 8 (▲) times with mixed P25/sol-gel TiO_2. Conditions: pH 6.4, $[As(III)]_{in}$ = 2.6 μM, $[NaNO_3]$ = 5 mM, average residence time = 5.85 min.

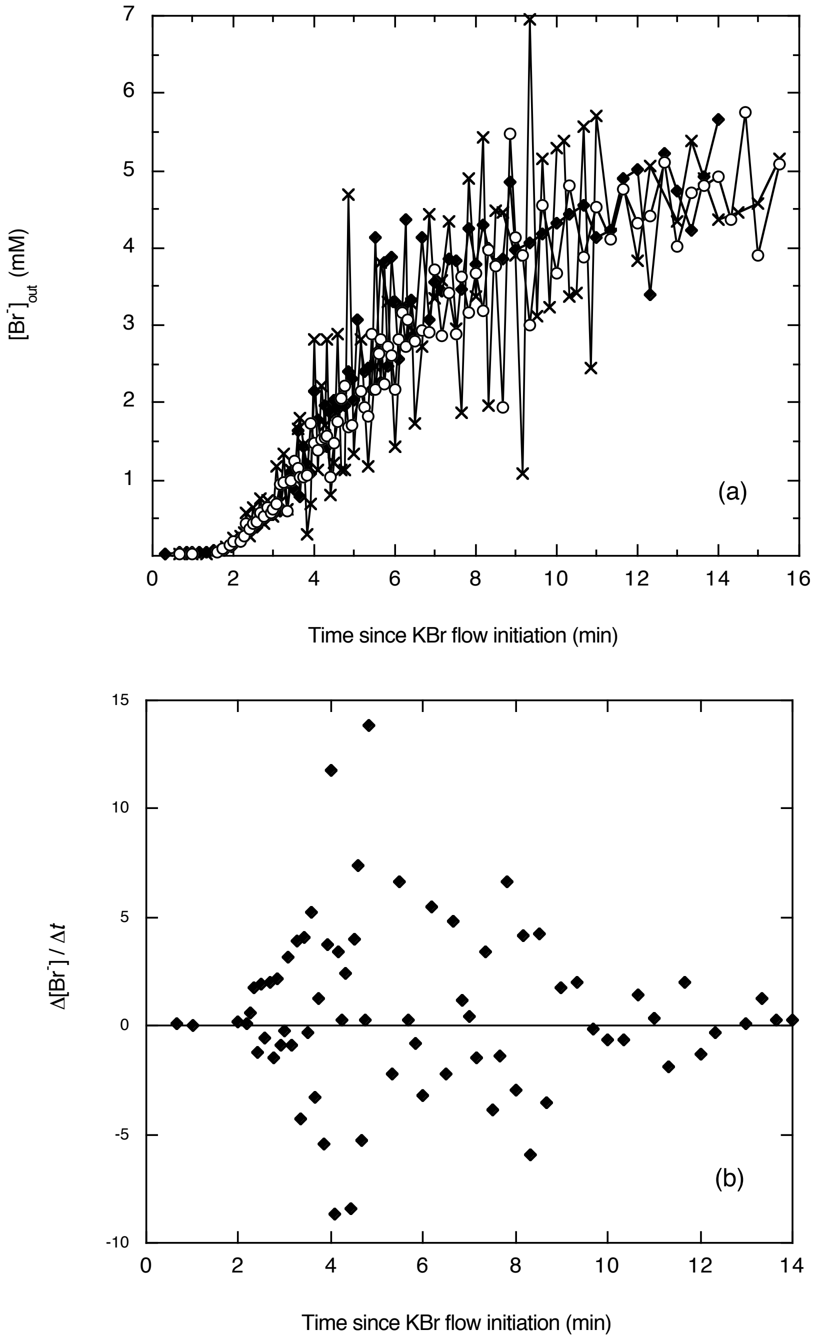

Figure A.7. Flow characterization of the reactor using a bromine-sensitive electrode (Orion) to measure $[Br^-]_{out}$. Reactor was first equilibrated with 0.05 mM KBr solution which was substituted by a 5 mM KBr influent solution at time = 0. The Br-sensitive electrode could not measure the effluent directly; instead it was placed in 50 mL of 0.05 mM KBr solution into which effluent dripped, and the change in $[Br^-]$ was used along with the reactor flow rate to calculate effluent $[Br^-]$. Three replicate experiments were conducted (a) and averaged. Average values of $\Delta[Br^-] / \Delta t$ are plotted in (b).

Appendix B

CALCULATIONS FOR TOTAL BED VOLUMES TREATED BY MIXED P25/SOL GEL-COATED BEADS

Beads used in the 22 hour (1307 minutes) $NaNO_3$ experiment (residence time = 15.56 minutes) were also used in 7 previous experiments, each of which resulted in 3 hours of UV exposure. Five of these experiments operated under fast flow conditions (residence time = 5.85 minutes), and the remaining 2 experiments experienced medium and slow flow rates corresponding to residence times of 10 and 15.56 minutes. The sum of the bed volumes treated in all experiments by this batch of beads yields

$$5 \times (180 / 5.85) + (180 / 10) + (180 / 15.56) + (1307 / 15.56)$$

$$= 267 \text{ total bed volumes}$$

Beads used in the 24 hour (1437 min) synthetic groundwater experiment were used in 2 previous groundwater experiments (both 3 hours long). All three experiments used a flow rate corresponding to a 10 minute residence time, so the number of bed volumes treated by these beads was

$$2 \times (180 / 10) + (1437 / 10)$$

$$= 180 \text{ total bed volumes}$$

Appendix C

PREPARATION OF P25-COATED BEADS

A slurry of P25 TiO_2 (12.3% by weight) was used for all coatings. The slurry was sonicated for 20 minutes before pouring over beads, allowing it to contact all sides of the beads, and decanting. To minimize caking, a 13-gauge needle was used to blow off excess TiO_2 with house air before placing beads in a laminar flow hood to dry. This process was repeated 1–5 times depending on how many coatings were desired. After the final coating, beads were placed in a furnace and heated at 300 °C for one hour. After cooling, beads were rinsed several times with deionized water to remove loosely bound TiO_2 and left to air dry.

P25-coated beads were used in preliminary flow-through experiments in a single-chamber reactor that was later modified into the 2-chamber reactor depicted in Appendix A. Small amounts of TiO_2 were observed to detach from the beads when they were picked up or jostled, even after multiple uses.

Appendix D

EFFECT OF POTASSIUM SUPEROXIDE ADDITION TO AS(III) OXIDATION IN A HOMOGENEOUS MEDIUM

D.1 Introduction

One of the primary arguments used against a possible As(III) photooxidation mechanism involving superoxide is the slow reaction kinetics between As(III) and superoxide in homogeneous solution (Xu et al. 2005). It was therefore desirable to determine if superoxide can oxidize As(III) on a time scale comparable to photocatalyzed oxidation experiments. Also, since superoxide is thermodynamically capable of both oxidizing As(III) (forming H_2O_2 as a reaction product) and reducing As(V) (forming O_2 as a reaction product), it was necessary to consider both of these pathways. In this study, the oxidation and reduction of As(III) and As(V) were examined using potassium superoxide (KO_2) as the source of superoxide.

D.2 Materials and Methods

The procedure followed in these experiments was adapted from Marklund (1976). A KO_2 pellet (Aldrich) with mass 50–100 mg was dissolved in 25 mL ice-cold 50 mM NaOH, resulting in considerable bubbling as approximately 60% of the superoxide disproportionated and released oxygen into solution:

$$2\,O_2^{\bullet -} + 2\,H^+ \rightarrow H_2O_2 + O_{2(g)} \qquad (D.1)$$

This stock solution was immediately diluted 1:80 in solutions containing 1.0 μM As(III) ($NaAsO_2$, Baker Analyzed) or As(V) ($Na_2HAsO_4{\bullet}7H_2O$, Sigma) adjusted to pH ~2.9 using HNO_3. After a 10 min reaction period, the solution pH was adjusted to 4.2–7.5 and As speciation was determined using anion exchange filters (3M Empore) and inductively coupled plasma mass spectrometry (Chapter 3).

D.3 Results and Discussion

The pH values in these experiments were highly variable because the KO_2 stock solution had an initial pH of 12.7 (0.05 M NaOH) and became increasingly basic as protons were consumed by superoxide dismutation. Experiments were designed to neutralize the strong base with strong acid, but slight mismatches resulting from variable amounts of superoxide disproportionated at the exact time of addition to As solution resulted in substantial departures from neutrality. This problem was the likely cause of poor reproducibility among replicate samples (Fig. D.1).

As(III) was oxidized in progressively greater concentrations as solution pH increased from 3.2 to 8.8 (Fig. D.1). In addition, at low pH, samples that initially contained As(V) were reduced by 30–45%, resulting in similar fractions of As(III) at pH 3.3 and 3.4 regardless of the initial oxidation state of As. These general pH trends are consistent with changes in As redox potentials.

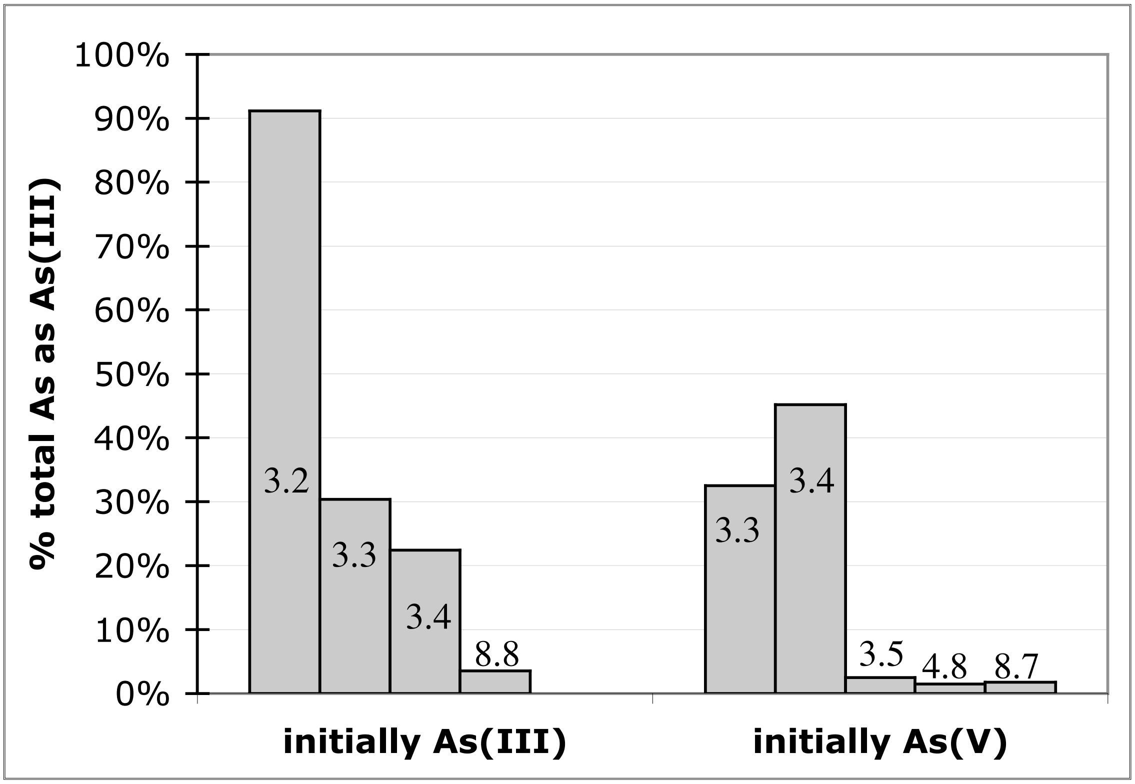

Figure D.1. Percent of total As present as As(III) 10 min after addition of KO_2 stock to 1 μM solutions of As(III) and As(V). Final pH values for each replicate sample are shown.

Since superoxide disproportionates into H_2O_2 and $O_{2(g)}$, the effect of H_2O_2 on As(III) oxidation must be considered. H_2O_2 has been shown to be unreactive with neutral H_3AsO_3 (Pettine et al. 1999), which is the dominant As(III) species below pH 9.2. Even considering the reaction of H_2O_2 with the monoanionic species $AsO(OH)_2^-$ yields no appreciable reaction: at pH 8.2, we can expect 0.1 μM of the 1.0 μM As(III) to be present as $AsO(OH)_2^-$, and in 10 min a reaction with 500 μM H_2O_2 would produce only 0.021 μM As(V) based on Pettine's rate constant:

$$AsO(OH)_2^- + H_2O_2 \rightarrow \text{products} \qquad k = 42\ M^{-1}\ min^{-1} \qquad (D.2)$$

500 μM H_2O_2 is the upper limit of H_2O_2 expected in these solutions. Therefore, the changes in As oxidation state with addition of KO_2 are attributed to reaction with superoxide.

Based on the pH dependence observed in Figure D.1, homogeneous oxidation of As(III) by superoxide would be substantial and reduction of As(V) would be insignificant at the pH values discussed in the rest of this work (6.3–8.3). Although the KO_2 system cannot be adjusted to adequately model the TiO_2-photocatalyzed system, the primary conclusions of this study are not inconsistent with a proposed mechanism of As(III) by superoxide.

Appendix E

VISIBLE LIGHT PHOTOOXIDATION OF AS(III) USING NITROGEN-DOPED TIO$_2$

* Performed as part of Asahi Okada's SURF research in summer 2004

E.1 Introduction

TiO_2 has many qualities that make it a valuable semiconductor photocatalyst, including its stability, biological and chemical inertness, and low cost. However, one drawback that prohibits broader applications of TiO_2 photocatalysis is its high bandgap energy, which restricts its activity to the ultraviolet (UV) region of the electromagnetic spectrum. Since UV irradiation accounts for only 3% of total solar flux, extending the active wavelength range of TiO_2 into the visible region would greatly increase its applicability. This is accomplished by creating energy levels within the band gap or by adjusting the potentials of the valence band or conduction band edges. Possible methods for achieving this goal include replacing lattice titanium with transition metal cations, creating oxygen vacancies, or replacing lattice oxygen with C, N, or S (Agrios et al. 2003) anions.

TiO_2 doped with nitrogen ($TiO_{2-x}N_x$) has been shown to absorb light up to 550 nm (Ihara et al. 2003). When irradiated with $\lambda > 400$ nm, it has been reported to degrade substrates including methylene blue in the aqueous phase (Asahi et al. 2001; Gole et al.

2004) as well as 2-propanol (Irie et al. 2003), acetone (Ihara et al. 2003), and acetaldehyde (Asahi et al. 2001) in the gas phase.

TiO_2 that is photoactive under visible light would greatly enhance the appeal of TiO_2-photocatalyzed As(III) oxidation in drinking water treatment applications. This appendix discusses the studies on As(III) photooxidation in visible light for nitrogen-doped TiO_2 prepared under a range of conditions.

E.2 Materials and Methods

E.2.1 Preparation of nitrogen-doped TiO_2

P25 TiO_2 and anatase TiO_2 (Aldrich) were heated to 300–900°C under a flowing mixture (~9 L hr^{-1}) of argon and ammonia gas (1:3 $Ar:NH_3$) for 1–24 hours. Following doping, selected samples were annealed with air in order to re-oxidize the surface. This involved heating under house air at 400–550 °C for one hour. Brunauer-Emmett-Teller surface area was determined using a Gemini 2360 Surface Area Analyzer.

E.2.2 Survey of photocatalytic activity

All prepared samples, undoped P25 and anatase, and 2 samples of iron-doped TiO_2 (previously prepared in Michael Hoffman's lab, Department of Environmental Science and Engineering, Caltech) were subjected to an initial test of photoactivity under visible light. 20 mL suspensions for batch slurry studies contained 0.05 g L^{-1} TiO_2, 0.005 M $NaNO_3$, and 3 μM As(III) and had an initial pH of 6.3 (adjusted using HNO_3 and

NaOH). Suspensions were prepared in borosilicate glass vials with Teflon-coated septa through which air was bubbled in and out. After slurries were stirred in the dark for 30 minutes to achieve sorption equilibrium, exposure to a 1000 W Xenon Arc lamp with output set to 500 W was initiated. Incident light was directed through 2 high pass filters (320 and 400 nm) and an IR filter. Samples were removed prior to irradiation and after 20 minutes of exposure to visible light. Subsequent filtration and analysis for As speciation was performed as described in Chapter 3. Results from this survey were used to choose which samples merited more detailed study.

E.2.3 Photocatalysis: Time series

200 mL sample suspensions (0.05 g L^{-1} TiO_2, 0.005 M $NaNO_3$, 3 μM As(III), pH 6.3) were prepared and transferred into a previously described cell (Chapter 3). Samples were removed intermittently over 2 hours of visible light irradiation during which the cell was kept at a constant temperature of 20 °C using a water jacket. Sampling and speciation analysis procedures were identical to those described in Chapter 3. Experiments were conducted over the wavelength ranges from 400 to 700 nm and 420 to 700 nm.

E.3 Results and Discussion

E.3.1 Characterization of nitrogen-doped TiO_2

Subsequent to heating under an NH_3/Ar atmosphere, nitrogen-doped samples ranged in color from blue-grey to black. After annealing, the TiO_2 became yellow or light green. Doped P25 samples had higher surface areas than doped anatase samples, and greater doping temperature or time (i.e., for annealing) were correlated with lower surface area (Table E.1).

Table E.1. Preparation parameters and surface areas of the nitrogen-doped TiO_2 samples.

Sample	**Doping Temperature (°C)**	**Doping Time (hrs)**	**Annealing Temperature (°C)**	**Surface Area (m^2 g^{-1})**
P25 Trial 1	500	3	500	38.6 (Annealed: 26.4/24.9)
P25 Trial 2	550	3	500	36.9
P25 Trial 3	900	1	Not annealed	26.9
P25 Trial 4	400	6	400	Not measured
P25 Trial 5	300	24	Not annealed	Not measured
Anatase Trial 1	550	3	550	7.7, 9.7 (Annealed: 7.6, 7.4)

E.3.1 Survey of photocatalytic activity

The fraction of As(III) remaining after 20 minutes of visible light exposure is shown in Figure E.1. No dramatic differences were observed between doped and undoped samples, but P25 Trials 4 and 5 both oxidized slightly more As(III) in 20 minutes than undoped P25. Similarly, anatase Trial 1 performed slightly better than undoped anatase, but more poorly than P25 samples. Activity of iron-doped samples was similar to that of the doped anatase but less than that of most P25 samples.

No consistent trends were observed on the basis of doping temperature, doping time, or solid surface area. Although annealed samples have performed better than non-annealed samples for other substrates, there was no significant difference in As(III) photooxidation between performance of annealed and nonannealed samples in these tests.

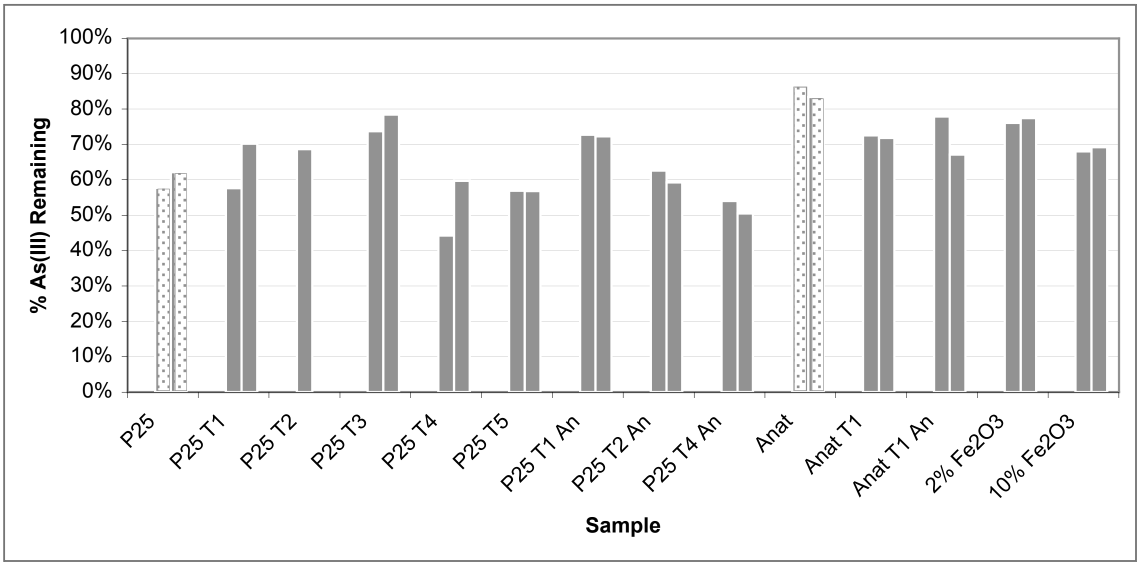

Figure E.1. Duplicate data sets showing percent of initial [As(III)] remaining unoxidized in solution after 20 min irradiation with 400 nm < λ < 700 nm. Undoped P25 and anatase samples are highlighted. T = trial, An = annealed, Anat = anatase. Conditions: $[As(III)]_0 = 3\ \mu M$, $0.05\ g\ L^{-1}\ TiO_2$, $0.005\ M\ NaNO_3$, pH 6.3, 500 W lamp intensity.

E.3.2 Photocatalysis: Time series

Both the annealed and nonannealed samples from P25 Trial 4 were chosen for more extensive photoactivity analysis. Photooxidation of all three samples was found to be pseudo first-order in dissolved As(III) concentration during irradiation with light in the range 400–700 nm (Figure E.2). Rate constants based on the first 60 min of As(III) oxidation were $0.025\ s^{-1}$ for both undoped P25 and nonannealed P25 Trial 4, whereas the annealed sample performed more poorly ($k = 0.011\ s^{-1}$).

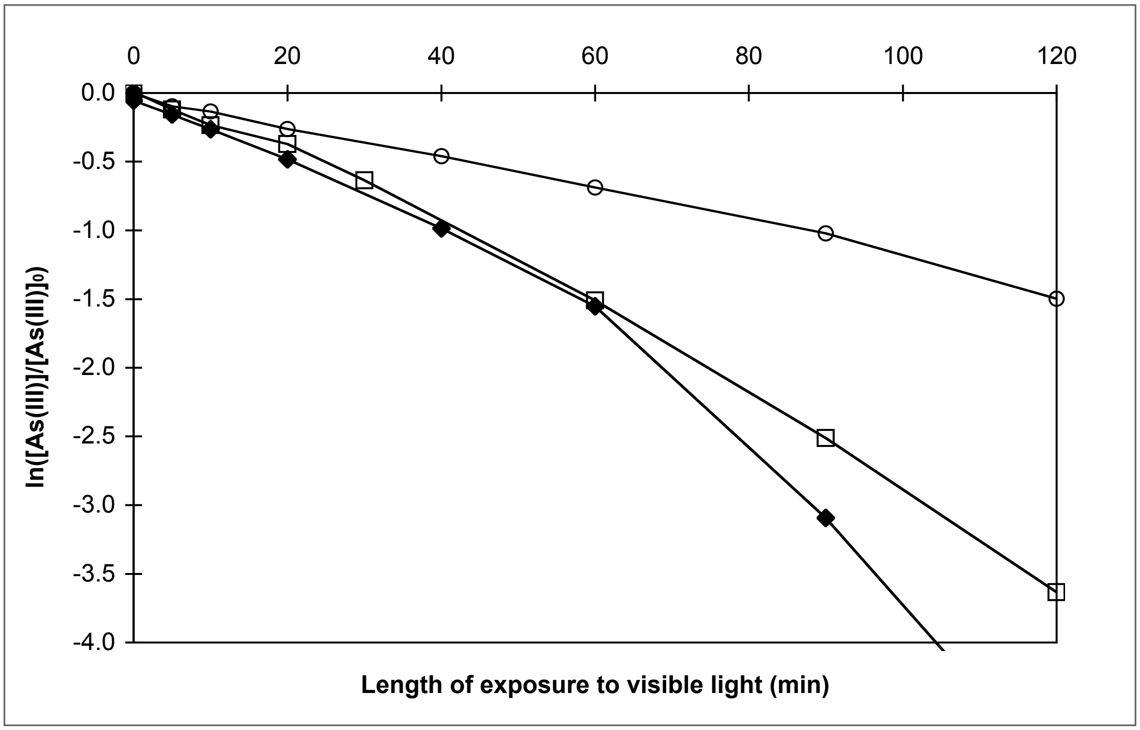

Figure E.2. Pseudo first-order loss of dissolved As(III) when using P25 (◆), N-doped P25 Trial 4 (☐), and N-doped P25 trial 4 annealed (○). Conditions: $[\text{As(III)}]_0 = 3\ \mu\text{M}$, $0.05\ \text{g L}^{-1}$ TiO_2, 5 mM $NaNO_3$, pH 6.3, 500 W lamp intensity.

These results suggest that despite the significant As(III) photooxidation observed under visible light, the nitrogen-doped TiO_2 offers no benefit over undoped TiO_2. Moreover, the near-complete loss of As(III) from solution within 90 min even for the undoped P25 sample was unexpected. The same concentration of As(III) would be oxidized under UV light within 10 min (Chapter 3), but undoped P25 should not be active in the visible region even at this much slower rate. It was hypothesized that this activity was due to P25's broad absorption tail, and that even though it is nominally inactive above 387 nm, a fraction of absorption is possible for wavelengths slightly above this cutoff. This was tested by performing similar experiments using 420 nm < λ < 700 nm, which showed that reactivity for both the undoped P25 and the P25 Trial 4 samples dropped substantially when the 400–420 nm wavelength range was eliminated. First order rate constants dropped to 0.003 s^{-1} for undoped P25 and 0.005 s^{-1} for Trial 4. Although limited data make it difficult to assess whether there is a significant difference between the rate constants of the doped and undoped samples under these conditions, is it clear that the nitrogen doping performed in this study did not enhance the reaction enough to make As(III) photooxidation viable in the visible range on the time scales necessary for water treatment.

One potential explanation for these results is that the doping procedure was not effective. Although no formal characterization of the doped powders was conducted, the doping procedure was based on previous studies (Asahi et al. 2001), including research with doped anatase using the same laboratory equipment (Mrowetz et al. 2004). In both of these studies, X-ray photoelectron spectroscopy and diffuse reflectance spectroscopy conducted for the doped material confirmed the presence of nitrogen within the TiO_2 matrix. Mrowetz et al. (2004) found that nitrogen-doped anatase samples were unable to catalyze the degradation of formate or hydroxylamine under visible light despite excellent activity under UV light. The authors observed no generation of hydroxyl radical under visible light and argued that previous experiments that successfully used $TiO_{2-x}N_x$ for visible light catalysis are not generally indicative of aqueous photocatalysis performance due to substrate selection and the differences between gas phase and aqueous phase reactions. This hypothesis is corroborated by the similar performance of undoped and nitrogen-doped TiO_2 observed in this study.